APPLIED SCIENCES AND ENGINEERING

Reversible adhesives with controlled wrinkling patterns for programmable integration and discharging

Yi Zhou[1,2], Lunan Yang[1], Zhen Liu[1], Yang Sun[1], Junfei Huang[1], Bingcheng Liu[1], Quan Wang[3], Leyu Wang[4]*, Yong Miao[1]*, Malcolm Xing[2]*, Zhiqi Hu[1]*

Switchable and minimally invasive tissue adhesives have great potential for medical applications. However, on-demand adherence to and detachment from tissue surfaces remain difficult. We fabricated a switchable hydrogel film adhesive by designing pattern-tunable wrinkles to control adhesion. When adhered to a substrate, the compressive stress generated from the bilayer system leads to self-similar wrinkling patterns at short and long wavelengths, regulating the interfacial adhesion. To verify the concept and explore its application, we established a random skin flap model, which is a crucial strategy for repairing severe or large-scale wounds. Our hydrogel adhesive provides sufficient adhesion for tissue sealing and promotes neovascularization at the first stage, and then gradually detaches from the tissue while a dynamic wrinkling pattern transition happens. The gel film can be progressively ejected out from the side margins after host-guest integration. Our findings provide insights into tunable bioadhesion by manipulating the wrinkling pattern transition.

INTRODUCTION

Fractal geometry proposed the essence of self-similarity, that is, a geometric shape can be generated using a simple iterative method (*1*, *2*). An abundance of fractal structures has been observed, such as meandering rivers, branching leaf veins, and curving cerebral cortices (*3*). These nontrivial geometric patterns contribute to pivotal biological functions, which increase surface-to-volume ratios and tend to maximize metabolic capacity (*4*, *5*). An ordered and self-similar structure is a promising model system for biomanufacturing.

Nature has evolved dynamic topographical surfaces to control adhesion and release (*6*). For example, fibrillar structures on the feet of gecko lizards enable robust, reversible, and directional adhesion by expanding their contact area (*7*, *8*). Beetles adhere to rough and waxy surfaces via mushroom-shaped architectures with wide concave tips on their forelegs (*9*). Surface patterns of wrinkling and buckling have been used in physics (*10*), electronics (*11*), and biology (*12*) to generate micro- and nanoscale structures with well-defined geometries and dimensions (*13*). In addition, surface patterns have been found to be associated with adhesion (*14*), but the generation of tunable surface wrinkling to control tissue adhesion is yet to be reported.

Tissue adhesives can overcome some issues in the sutures, where the time and the mechanical stress are sensitive (*15*, *16*). Bioadhesives are designed to quickly bridge the wound gap and form temporary barriers to prevent fluid leakage (*17*, *18*). In addition, tissue adhesives can be multifunctional by installing bioactive molecules (*19*, *20*) for hemostasis (*21*–*24*) and fast wound healing (*25*, *26*). However, current tissue adhesives are far from ideal. Natural or biological adhesives (e.g., fibrin-based and collagen-based adhesives) adhere weakly to tissues and are thus susceptible to rupture and debonding (*27*). Adhesives containing cyanoacrylate derivatives and catechol components (which require additional oxidation reagents or enzymes) provide sufficient strength but carry risks of cytotoxicity and potential contamination (*28*). Moreover, the degradation process of existing adhesives cannot be manipulated in real time, and the adhesion strength of current reversible bioadhesives is relatively low (*29*, *30*). With these in consideration, the synthesis of a safe, effective, and on-demand removable tissue adhesive remains challenging.

Inspired by nature and using buckling dynamics, we designed a wrinkle pattern transition on the gel adhesive film with acrylic acid (AA) and acrylamide (AM). The carboxylic acid groups in poly(AA) formed intermolecular bonds (hydrogen bonds and electrostatic interactions), and the primary amines in poly(AM) endowed the film with adhesiveness. Further in-depth investigation of the adhesion behavior revealed that the adhesion capacity was reversible and controlled by the wrinkling morphology. In addition, the film adhesive was demonstrated to be biocompatible and provided sufficient adhesion for tissue sealant in the skin flap model. The film adhesive could also play a role in drug delivery and promoted the survival of the skin flap. Last, it could be mechanically ejected from the wound after gradual detachment from the tissue.

RESULTS AND DISCUSSION

Fabrication of film adhesive and pattern characterization

The film adhesive was synthesized using AA and AM (Fig. 1, A and B, and fig. S1). According to the Fourier transform infrared (FTIR) spectra in Fig. 1C, the bands of O—H and N—H (at approximately 3100 to 3500 cm^{-1}) clearly indicate poly(AA-co-AM) [p(AA-co-AM)] formation, which may be closely related to the formation of hydrogen bonds. The wide absorption bands (at approximately 2400 to 2600 cm^{-1}) are attributed to the —OH from the carboxylic group. The stretching vibrations of the C—H, C—O, C—N, and

[1]Department of Plastic and Aesthetic Surgery, Nanfang Hospital, Southern Medical University, Guangzhou 510515, P.R. China. [2]Department of Mechanical Engineering, University of Manitoba, Winnipeg, MB R3T 2N2, Canada. [3]School of Civil Engineering, Shantou University, Shantou 515063, P.R. China. [4]Guangdong Provincial Key Laboratory of Construction and Detection in Tissue Engineering, Biomaterials Research Center, School of Biomedical Engineering, Southern Medical University, Guangzhou, Guangdong 510515, P.R. China.
*Corresponding author. Email: malcolm.xing@umanitoba.ca (M.X.); huzhiqidr163@i.smu.edu.cn (Z.H.); miaoyong123@ i.smu.edu.cn (Y.M.); wangleyu889@163.com (L.W.)

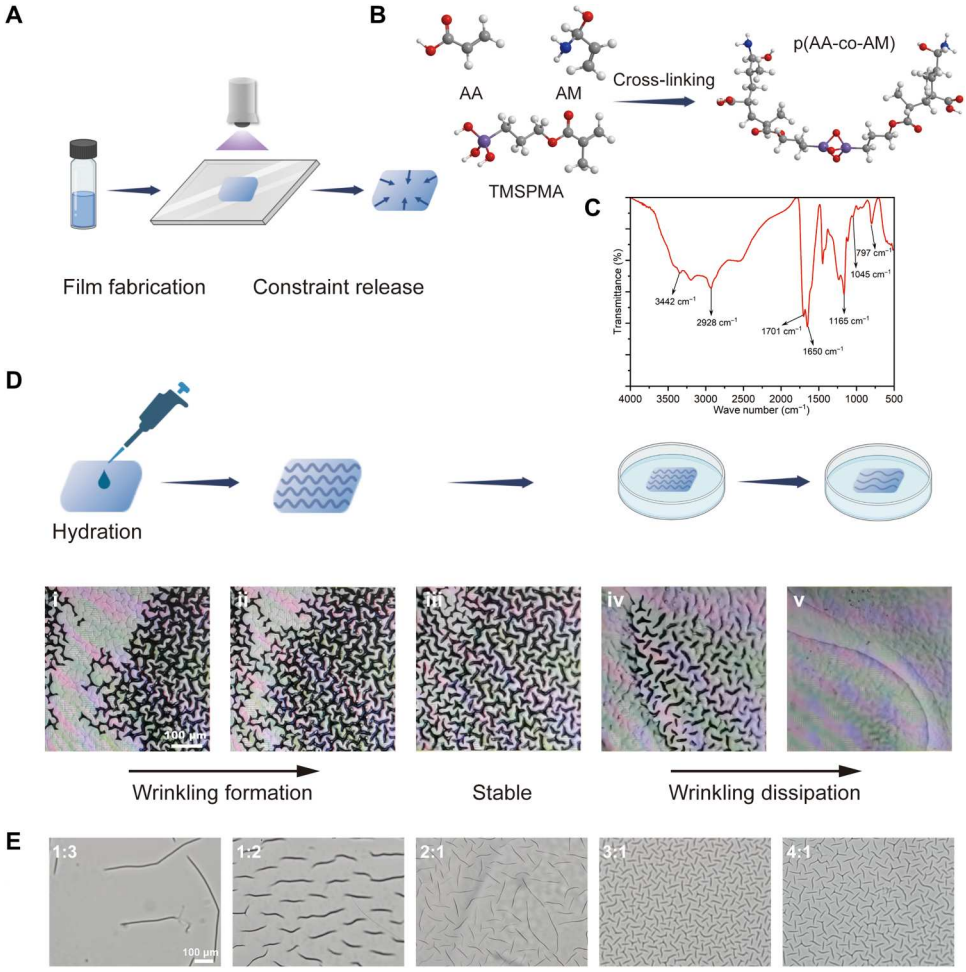

Fig. 1. Fabrication and characterization of the film adhesive. (**A** and **B**) AA, AM copolymerize, 3-(trimethoxysilyl)propyl methacrylate (TMSPMA), and the product p(AA-co-AM) copolymer cross-link into a network under ultraviolet light. (**C**) FTIR spectra of p(AA-co-AM) adhesive. (**D**) Schematic of wrinkling formation after hydration and wrinkling dissipation after immersed in water. Sequential photos of wrinkling formation (i to iii) and wrinkling dissipation (iv and v) (AA:AM = 3:1). Scale bar, 100 μm. (**E**) Optical microscopy images of stable wrinkling patterns after hydration with different proportions of AA and AM. Scale bar, 100 μm.

carbonyl groups are associated with bands found at 2928, 1165, 1412, and 1701 cm^{-1}, respectively (*31*). In addition, the characteristic peak of AM (amide I) is observed at approximately 1650 cm^{-1} (*32*). Furthermore, the spectra show a region around 1045 cm^{-1} corresponding to Si—O and 797 cm^{-1} associated with C—Si.

Previous work has demonstrated that the water content of a hydrated film can regulate wrinkling behavior (*33*). In our study, a dry hydrogel film was formed on a hard substrate; after the subsequent removal from the hard substrate, which triggered the release of residual stresses, it imbibed water [here phosphate-buffered saline (PBS)]. The wrinkling patterns were produced in seconds and remained stable (movie S1), which is consistent with the theory of wrinkling (*34*). Hydration of the sample occurred first on the surface, causing the formation of a surface "skin" on the gel film, which is much softer than the interior. As part of the film remained dry, the anisotropic stress caused surface wrinkling (*33*). After the entire film was immersed in water (here PBS), the wrinkles gradually smoothed out and disappeared, lastly regaining the flat pattern (Fig. 1D and movies S2 to S6). AA is an acidic anionic monomer with negatively charged carboxylic acid groups, inducing hydration of the hydrogel film (*33*, *35*, *36*). Hence, we investigated the effect of the molar fraction of AA in p(AA-co-AM) on wrinkling and adhesion behavior. Figure 1E shows a set of optical microscopy images of the wrinkled surface morphologies formed by adjusting the AA:AM ratio. With an increased proportion of AA, the wrinkling patterns changed from a random crack regime (ratio 1:3, 1:2, and 2:1) to an organized herringbone regime (ratio 3:1 and 4:1). In addition, the wrinkle intensity peaked at a ratio of 3:1 (≈400 wrinkles/mm^2) and then declined at 4:1 (≈270 wrinkles/mm^2). Therefore, a ratio of 3:1 was considered the optimal proportion for the formation of intensive and organized wrinkling patterns. The surface wrinkling pattern was reversible during the hydration-drying cycle (fig. S4). In addition, the molar fraction of AA determined the swelling ratio. In the swelling test, the adhesive reached an equilibrium state after approximately 12 hours, with a swelling ratio of 11.5% in the film area (AA:AM at 3:1; Fig. 2A).

Adhesion performance of gel film with skin tissue

Upon contact with wet tissues, adhesives based on AA rapidly remove the interfacial water, and the repeating carboxylic acid

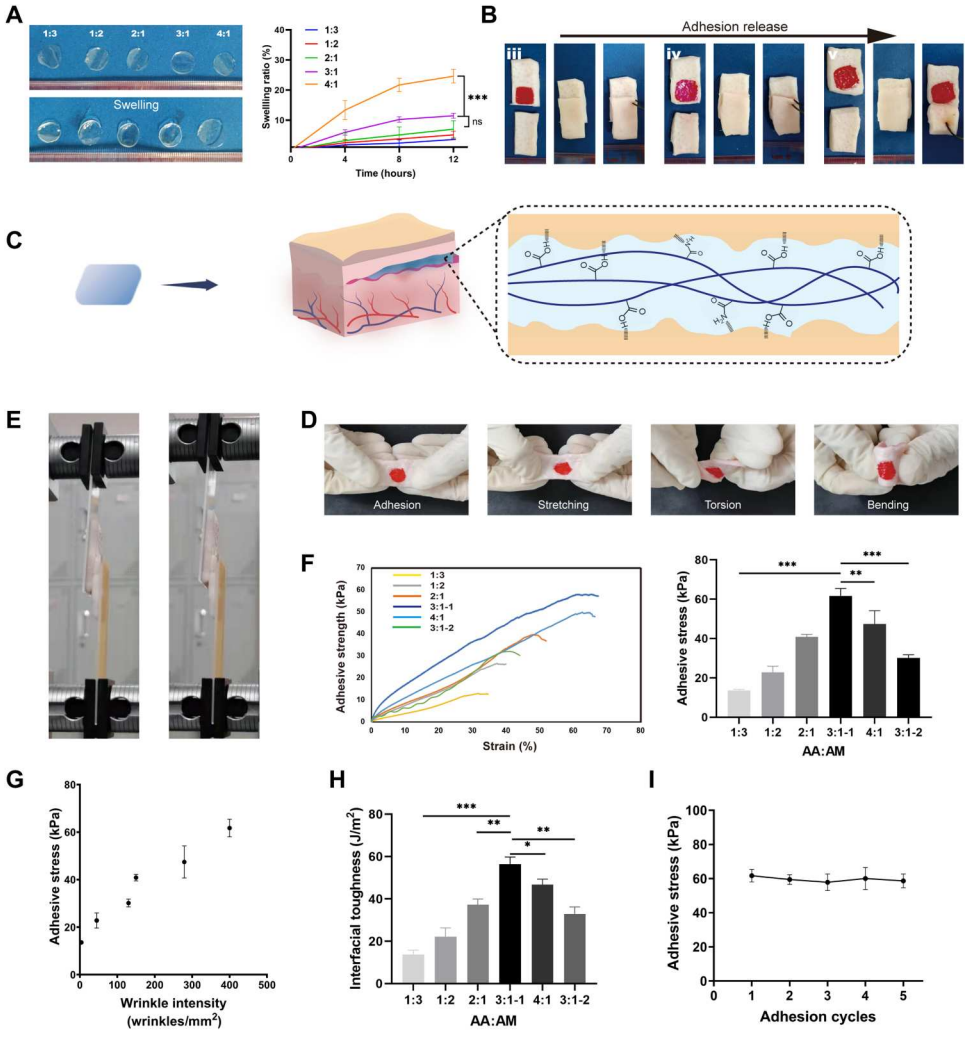

Fig. 2. The adhesion performance of gel film with skin tissue. (**A**) Representative photographs and swelling ratio of the films after immersion in PBS solution for 12 hours. ns, not significant. (**B**) The adhesive capacity decreased in accordance with the dynamic wrinkling pattern of Fig. 1D (iii to v). (**C**) The film could firmly adhere to skin tissue by hydrogen bonds under stretching, torsion, and bending (**D**). (**E**) Representative photographs of porcine skin under shear adhesion test. (**F**) Stress-strain curves and adhesive stress of samples with different proportions of AA and AM. (**G**) Relationship between wrinkle intensity and adhesion strength. (**H**) Interfacial toughness of the film adhesive on porcine skin. (**I**) Reversible adhesive property of the film adhesive on porcine skin. *$P < 0.05$, **$P < 0.01$, and ***$P < 0.001$.

functionality contributes to the high density of hydrogen bonds, thus achieving adhesion (*36*). In addition, the wrinkling patterns increase the possibility of surface interaction with skin tissue, which could effectively enhance the adhesive strength. Here, we chose porcine skin as the model tissue to explore the tunability of adhesion properties. The film adhesive showed rapid and robust adhesion with the skin tissue (Fig. 2, Biii, C, and D, and movie S7). After immersion in water (here PBS), the adhesive capacity decreased (Fig. 2B, iv and v) when the surface morphology changed from wrinkled to wrinkle-free (Fig. 1D, iv and v). We then quantified the adhesive strength of the film on porcine skin with different compositions of AA and AM by shear adhesion tests (Fig. 2E and movie S8). A general trend was determined in which the adhesion capacity increased with wrinkle intensity. The samples with the most intensive wrinkling pattern (3:1-1) exhibited superior adhesive capacity compared to all other samples (Fig. 2F). The adhesive strength reached 61.7 ± 3.7 kPa, which was significantly larger than that of the other samples ($P < 0.01$), as well as fibrin glue (24.0 kPa) (*37*). We also compared the film adhesive with other switchable bioadhesives, and the film adhesive we designed showed the superiority in adhesion strength (fig. S5) (*38*–*54*). Thus, we fixed the ratio of AA to AM at 3:1 for the subsequent in vivo experiments. Similar to the adhesion mechanism of geckos and wrinkles on octopus suction cups (*55*), the film adhesives with wrinkled surface increase the contact area at the mesoscopic scale (*56*). In addition, the wrinkled surface could provide flexibility or increase the friction coefficient, both of which could improve the adhesive performance. The film immersed in water (3:1-2) with the pattern of Fig. 1Div (≈130 wrinkles/mm^2) was also detected, and the adhesive stress decreased by approximately twofold (30.1 ± 1.6 kPa; Fig. 2F). The relationship between wrinkle intensity and adhesion strength was presented in Fig. 2G, which indicated that tissue adhesion was tailored by surface wrinkling patterns. The adhesion energy of the film adhesive on porcine skin tissue

was also evaluated, as shown in Fig. 2H. The sample (3:1-1) exhibited excellent interfacial toughness, reaching 56.4 ± 3.4 J/m^2. The dynamic and reversible nature of hydrogen bonding interactions contributes to reversible adhesion capacity of the film adhesive (*57*), and we detected that the adhesion strength remained almost the same ($P > 0.05$) over 5 cycles (Fig. 2I).

Switchable adhesion with controllable wrinkling wavelength

To further analyze the wrinkling patterns in the bilayer composite system, the film adhered to the skin was observed using scanning electron microscopy (SEM) (Fig. 3A). At the ratios of 1:3, 1:2, and 2:1, the film exhibited an irregular wrinkling pattern (Fig. 3C). When the molar fraction of AA reached and exceeded 0.75 (3:1 and 4:1), the film presented stripe-patterned wrinkles (with wavelengths ≈8 and 14 μm, respectively; Fig. 3, B and C, and fig. S6). Next, we focused on the change in the surface patterns at a ratio of 3:1, as shown in Fig. 3B. Initially, the film exhibited a completely flat and smooth surface topography (stage 0). When adhered to the skin tissue (stage 1), the surface wrinkles present in a self-similar periodic pattern, as short- and long-period wrinkles, were simultaneously observed on the film. The wavelengths of the stripe wrinkles were ≈0.8 and 8 μm, respectively.

According to the reported model of a bilayer composite system for surface wrinkling, the wavelength is determined by minimizing the force in the force equilibrium (*58*, *59*)

$$\overline{E}_f I \frac{d^4 z}{dx^4} + F \frac{d^2 z}{dx^2} + kz = 0 \quad (1)$$

$$I = \frac{wh^3}{12} \quad (2)$$

$$k = \frac{\overline{E}_s w \pi}{\lambda} \quad (3)$$

where I is the moment of inertia, w is the width of the film, and h is the film thickness. F is the compressive stress between the film and skin, and k is the Winkler′s modulus of an elastic half-space. The z axis is defined to be normal to the surface, and the x axis is parallel to the direction of F. In this study, h (12 μm) is the film thickness. E_f (≈ 270 kPa), ν_f (0.3), E_s (25 MPa), and ν_s (0.5) (*60*) represent the Young′s modulus and Poisson′s ratio of the film (subscript f) and the substrate (subscript s), respectively.

$$\overline{E}_f = E_f/(1 - \nu_f{}^2) \quad (4)$$

$$\overline{E}_s = E_s/(1 - \nu_s{}^2) \quad (5)$$

$$\lambda = 2\pi h \left(\frac{\overline{E}_f}{3\overline{E}_s}\right)^{\frac{1}{3}} \quad (6)$$

On the basis of Eq. 6, the observed wavelength of the long-period wrinkle approximates the theoretical value (≈9 μm). In addition, the equation indicates that the thickness and modulus of the film adhesive profoundly affect the wrinkling behavior, while the parameters are determined by the water absorption. Therefore, the surface wrinkling pattern keeps changing with the exudation of tissue fluid and swelling of the film adhesive. When the bilayer system was immersed in PBS to mimic tissue fluid exudation in vivo before fixation with glutaraldehyde (stage 2), the striped wrinkles become shallow, with waves merging and deep boundary appearing between the short-period wrinkles (Fig. 3B).

The formation of surface wrinkles represents the self-organization driven by instability, and examples are common in natural systems, such as aging human skin, brain cortex, and dried fruit (*11*, *61*–*63*). The dynamic wrinkling morphologies are able to regulate the physical, biological, and physiological functions (*64*). Therefore, many efforts have been devoted to construct reconfigurable hierarchical wrinkling patterns for realizing smart surfaces. Wrinkles occur by minimizing the total potential energy stored in the film when the residual stresses exceed a critical value (*59*). The residual stresses can be induced by thermal expansion (*65*, *66*), swelling (*59*, *67*), mechanical stretching, or compression (*68*, *69*). The wrinkling pattern is a compromise between the bending energy and standard deformation energy (*61*). This is similar to the wrinkling of our skin, which is the result of different mechanical properties between the thin, relatively stiff epidermis and the thick, soft dermis (*61*).

In this study, the film imbibes the interstitial fluid and then swells, while the tissue tends to maintain its original state, thus performing compressive stress on the swollen adhesive. After the formation of primary short-wavelength wrinkles, further stretching causes the amplitude of these wrinkles to grow until saturation, which makes the film thicker than the original film. This film wrinkles on larger wavelength scales, forming a hierarchical self-similar pattern (*33*).

In addition, the interaction of the adhesive film with skin tissue was assessed using hematoxylin and eosin (H&E) staining and SEM images. In stage 1, the film was tightly adhered to the skin tissue entangled with the collagen fibers in periodic wrinkles (Fig. 3, D and F), whereas after liquid infiltration, cracks were observed between the film and collagen fibers, indicating gradual detachment as wrinkling patterns became flattened (Fig. 3, E and G).

Biological safety and activity of the film adhesive

Biocompatibility is a prerequisite for the application of tissue adhesives, and the film adhesive is suitable for drug delivery. Here, we coated the adhesive with vascular endothelial growth factor (VEGF), an angiogenic factor specific for vascular endothelial cells that can promote angiogenesis and increase vascular permeability, to fabricate p(AA-co-AM)-VEGF. We then cultured fibroblast cells (FBs) and human umbilical vein endothelial cells (HUVECs) with p(AA-co-AM) and p(AA-co-AM)-VEGF in a Transwell system to evaluate the cellular response to the dry film adhesive (Fig. 4A). According to cell counting kit 8 (CCK8) quantitative detection, the adhesive showed no cytotoxicity in either cell type during the 48-hour treatment, while p(AA-co-AM)-VEGF significantly promoted the proliferation of HUVECs ($P < 0.05$; Fig. 4B). Live/dead staining performed on days 2 and 4 also showed that the cells remained at good activity levels with rare dead cells (Fig. 4C). These results indicate that the dry film adhesive could be applied in vivo.

As VEGF was loaded onto the surface of the adhesive followed by freeze-drying, it showed a burst release in the first 24 hours at about

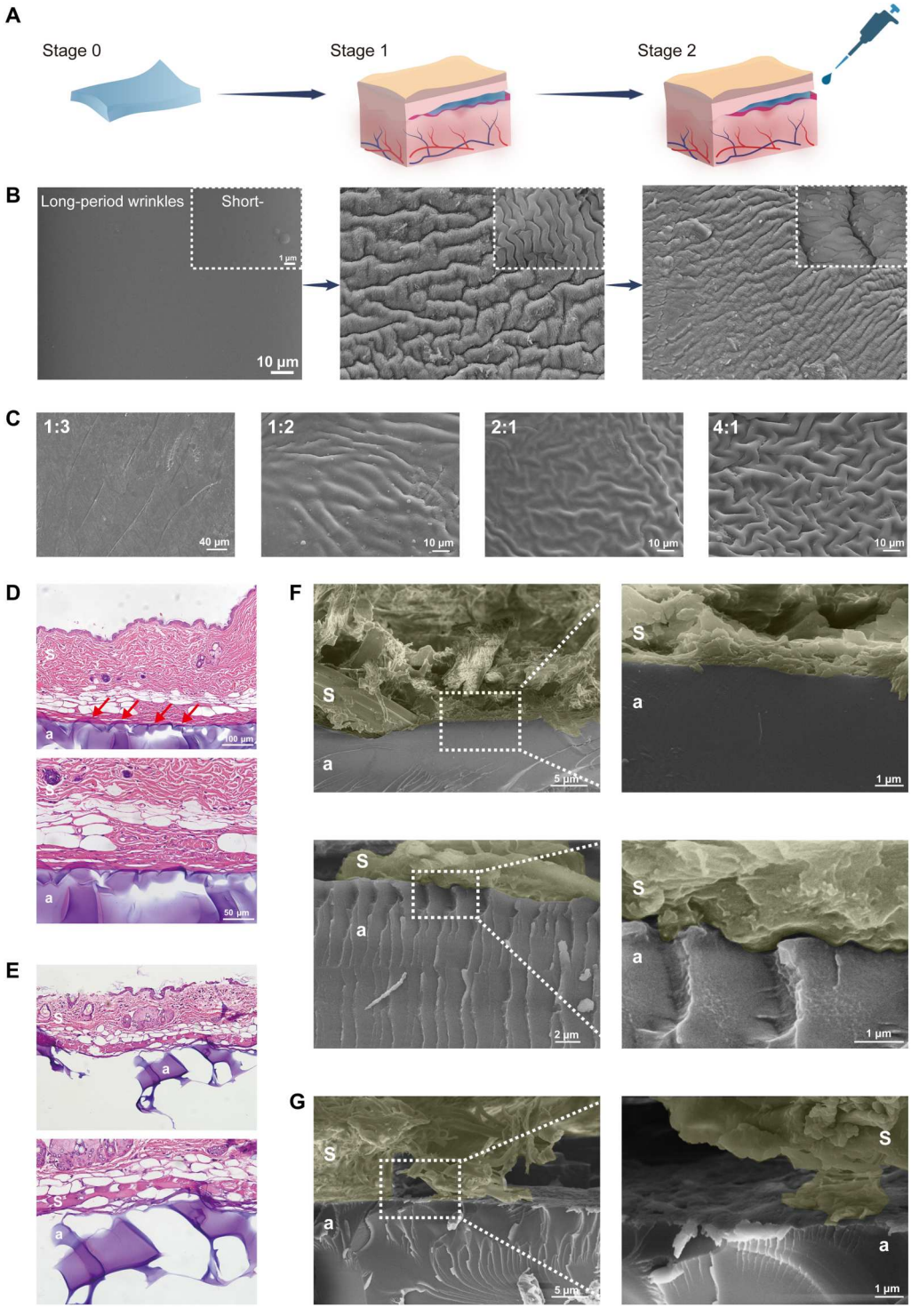

Fig. 3. Microscopic observation of dynamic wrinkling patterns and interaction between the film adhesive and skin substrate. (**A**) Schematic illustration of sample preparation. The film (stage 0) is adhered to skin tissue (stage 1), and then PBS is added to mimic tissue fluid exudation in vivo (stage 2). (**B**) Hierarchical dynamic wrinkles (long- and short-period wrinkles) at the ratio of 3:1 at the above three stages. (**C**) SEM images of surface wrinkling patterns on the film adhesive at different proportions of AA and AM. (**D** and **E**) Hematoxylin and eosin (H&E) staining and (**F** and **G**) SEM scanning of the interface. (D) and (F) The film tightly adhered to the skin with wrinkles (indicated by red arrows), which became flattened during the (E) and (G) debonding process. S, skin; a, adhesive.

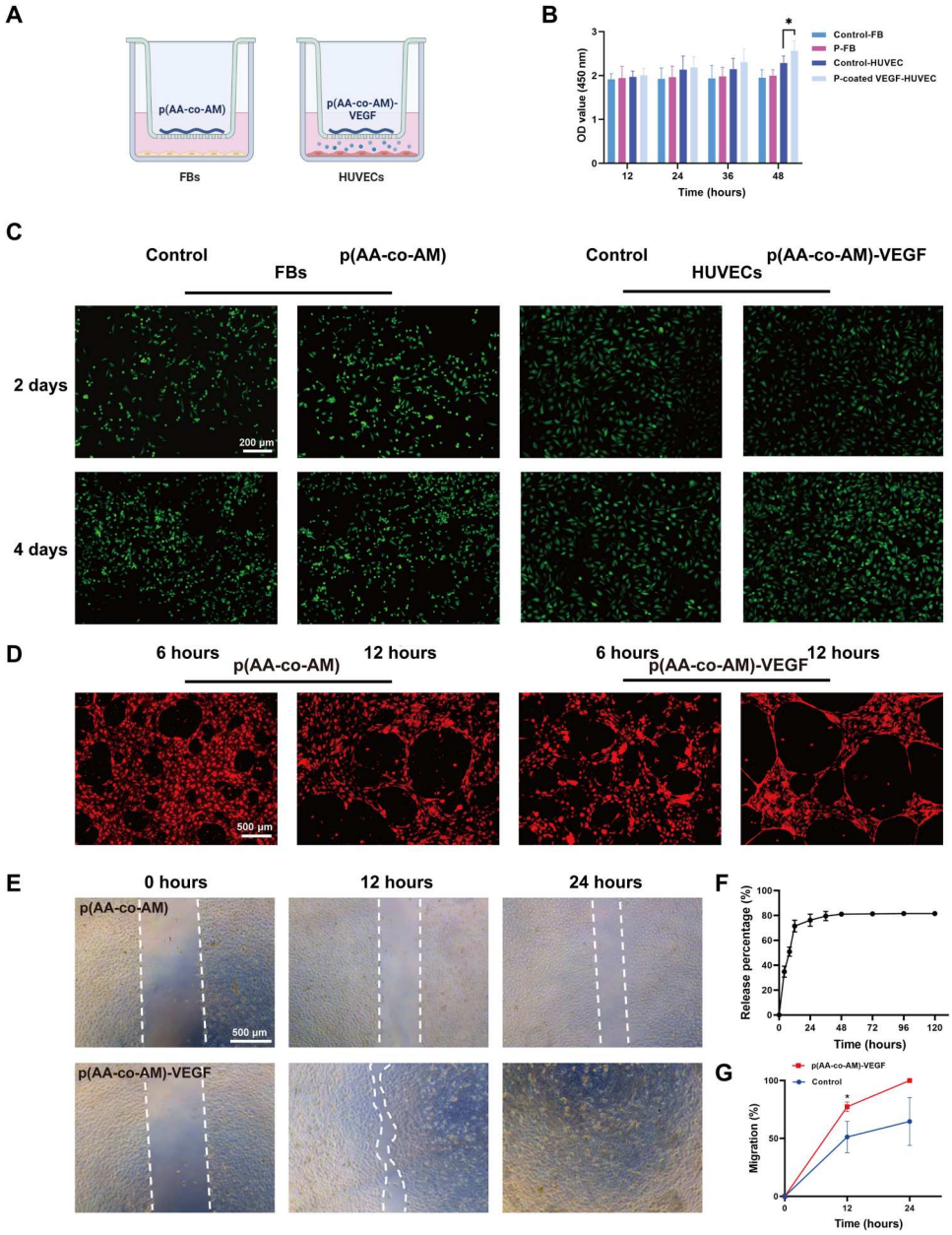

Fig. 4. Biocompatibility and bioactivity of the film adhesive. (**A**) Schematics depicting FBs and HUVECs culture with p(AA-co-AM) or p(AA-co-AM)-VEGF in the Transwell system. Cells without treatment were cultured as a control. (**B**) The proliferation of FBs and HUVECs was measured by CCK8 assays at different time points. OD, optical density. (**C**) Live/dead staining of FBs and HUVECs on days 2 and 4. (**D**) Tubule formation assay showing the effect on in vitro angiogenic capacity of HUVECs. (**F**) Release profile of VEGF from the adhesive. (**E** and **G**) Images of HUVECs migration after the scratch assay and the quantitative analysis. *$P < 0.05$.

76.2 ± 4.9% and the curve tended to be stable at 48 hours with a final release of 81.1 ± 0.7% (Fig. 4F). By fitting the drug release profile to the Ritger-Peppas equation, we obtained $M/M_{inf} = 56.95\ t^{0.08}$, indicating that the drug release mechanism conforms to Fick's law of diffusion (*70*). As shown in Fig. 4D, HUVECs treated with p(AA-co-AM)-VEGF showed tubule formation at 6 hours with a more extended network of tubules at 12 hours, which was barely observed in the control group at the same time point. Further, an in vitro scratch assay indicated that p(AA-co-AM)-VEGF treatment promoted endothelial cell migration, and after 24 hours of treatment, the scratch incubated with p(AA-co-AM)-VEGF completely disappeared, whereas it could still be clearly observed in the control group (Fig. 4, E and G). These results indicate that VEGF released from the adhesive maintained bioactivity and accelerated the proliferation, tubule formation, and migration of endothelial cells.

Functional adhesion and detachment for skin flap survival

To verify the potential of the reversible bioadhesive, we established a mouse model of random skin flap transplantation, an important method for severe wound repair (*71*). Tissue adhesive may be a

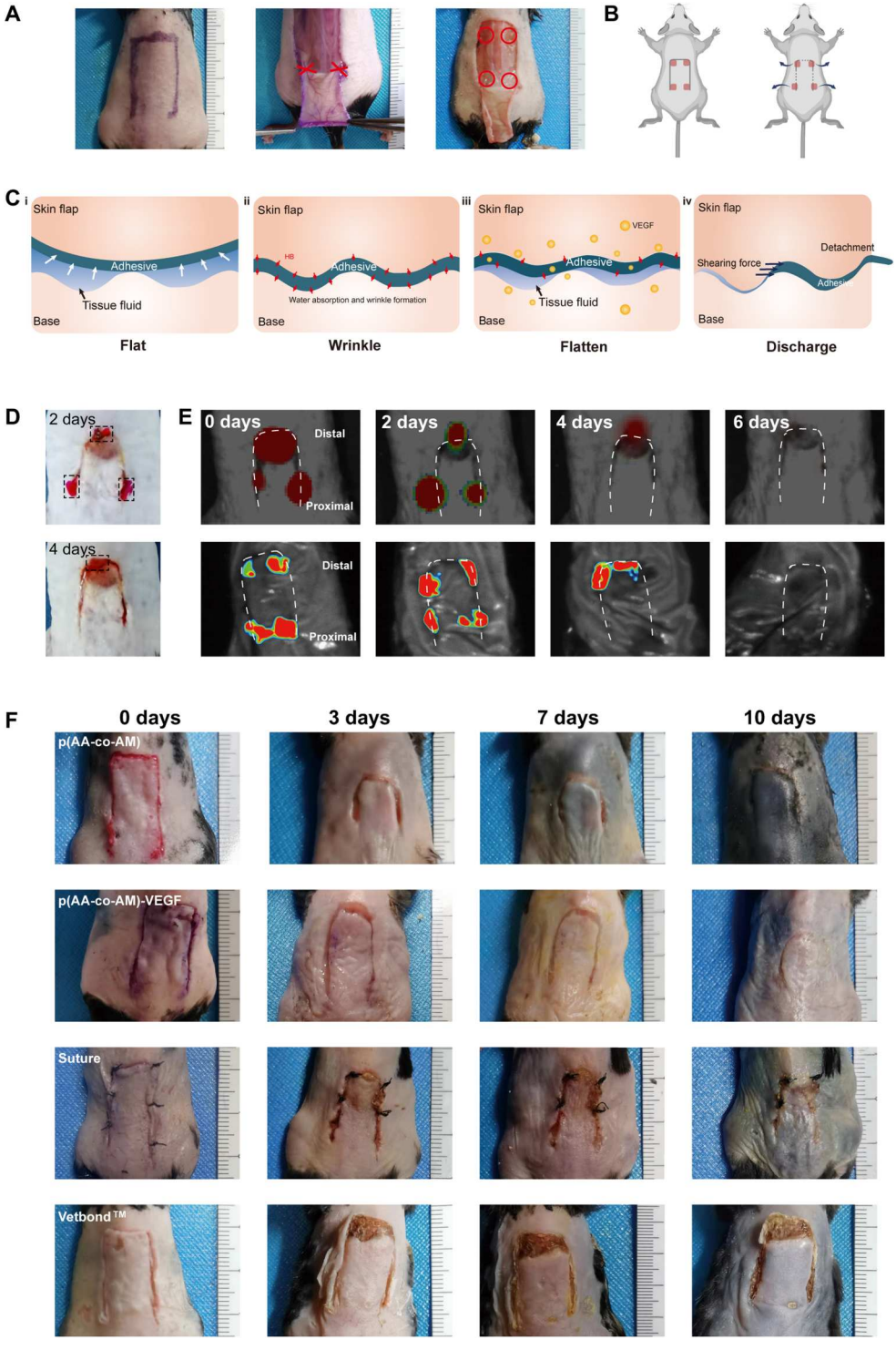

Fig. 5. Programmable adhesion and detachment for skin flap survival. (**A**) Preparation of the skin flap model. All perforator arteries beneath the flap, including bilateral deep circumflex iliac vessels, were cut and the dry film adhesives were deposited on the edges of the flap (indicated by four red circles). (**B**) Schematic illustrations and (**C**) mechanism of the film adhering to and detaching from the skin with the exudation of tissue fluid. HB, hydrogen bond (black dotted borders indicate the discharged films and white dotted borders indicate the flap edges). (**D**) General photographs and (**E**) in vivo fluorescence imaging showed the location change and final detachment of the film adhesive 6 days after surgery. (**F**) Postoperative images of skin flap models 10 days after treatment.

promising application to shorten the operation time and rapidly recover blood perfusion. Four pieces of film adhesive were placed on the edges of the flap for stable fixation to substitute for traditional suturing (Fig. 5A). In addition, the adhesives were designed to be sufficiently small to avoid adverse effects on the blood supply from the base.

Now, some polymeric tissue adhesives focus on enhancing the adhesion capacity while overlooking the detachment aspect (*72*). The bioadhesives with on-demand removable capabilities have been demonstrated superior in tissue regeneration (*73*–*75*). In this study, the dynamic regulation of hierarchical surface wrinkling patterns enabled the control of surface attachment. Rhodamine B–labeled adhesives were used to track the internal adhesion in vivo, presenting the bonding, debonding, and final ejection process in mice (Fig. 5B). When applied in vivo, the film adhesives immediately absorbed tissue fluid and offered sufficient adhesion with an intense surface wrinkling pattern (Fig. 5C, i and ii). With the sustained exudation of the interstitial fluid, the continuous hydration of the gel film caused the compressive stress to change; thus, the wrinkles became flattened with a decline in adhesion capacity (Fig. 5Ciii). Meanwhile, the healing process between the host and guest generated a force; when the forces were larger than the weakened adhesive force, the thin film was lastly extruded spontaneously from the interfaces (Fig. 5Civ). The proximal part was ejected within 4 days, as the proximal part regenerates faster than the distal part. Subsequently, all adhesives were discharged automatically on day 6, while at that time, the flaps were integrated with the host (Fig. 5, D and E). The mechanical loading of an in vivo microenvironment led to the driving force for detachment without any additional chemicals or harsh triggers, and detachment was compatible with tissue healing to avoid the problem of wound rupture or prolonged inflammation.

In skin flap transplantation, flap necrosis is still an unsolved common postoperative complication. Hence, the stimulation of neovascularization in the early phase plays a central role in flap survival (*76*). Angiogenic growth factors have been demonstrated to improve flap perfusion but are limited by the lack of a feasible delivery system with controlled release (*77*). The release profile of p(AA-co-AM)-VEGF was consistent with the vital period of vascular reconstruction in the skin flap (Fig. 4F); thus, it was used to enhance vascularization (*78*). Clinically used suturing and Vetbond adhesive were used as controls. Postoperative images of

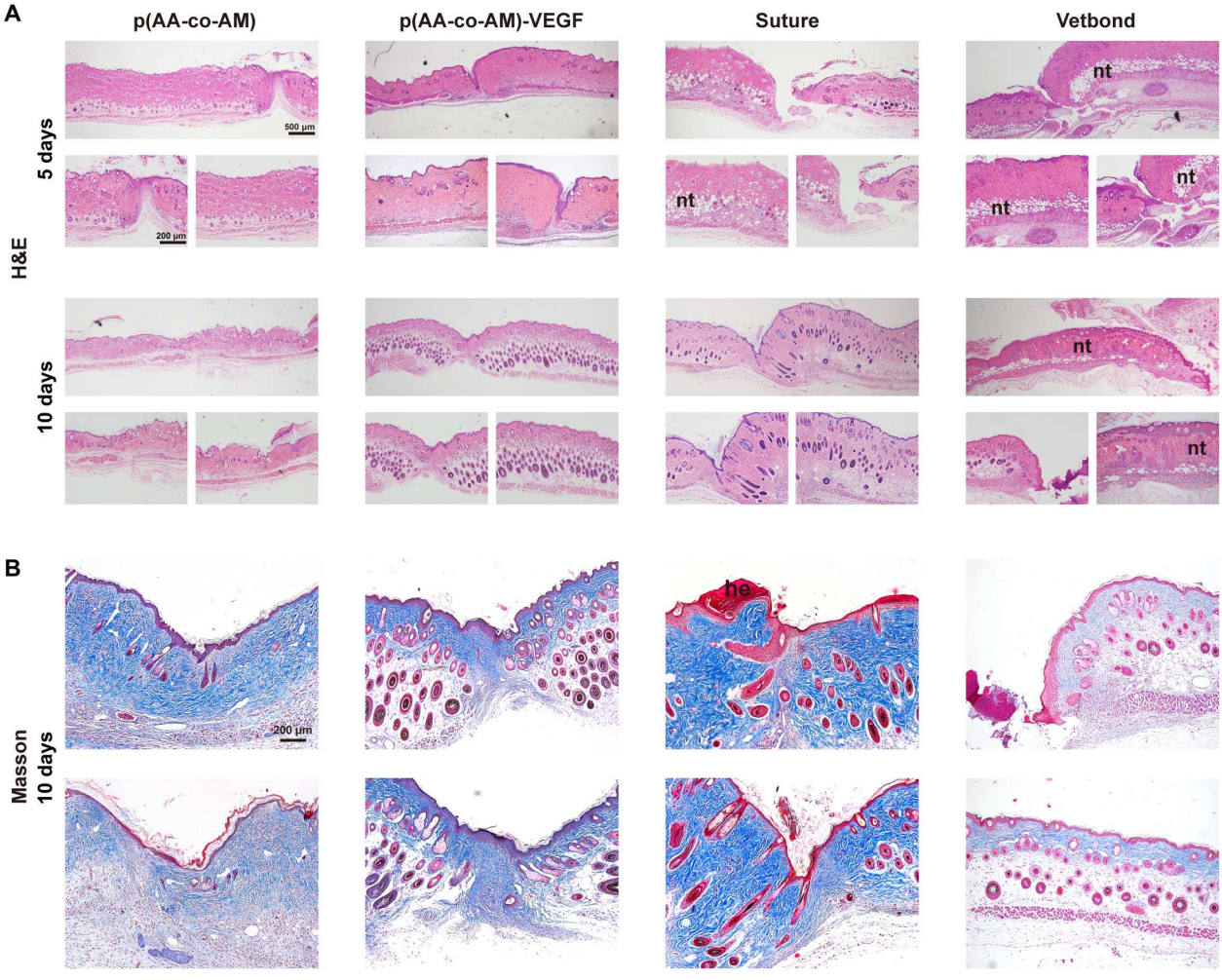

Fig. 6. Histological analysis of the margins of defects in skin flaps. (**A**) H&E staining sections showing the integration of the side margins of the flap defects on postoperative day 5 and 10 and (**B**) Masson's trichrome staining of each group on day 10. nt, necrotic tissue; he, hypertrophic epidermis.

the skin flap in each group are shown in Fig. 5F. The skin flaps treated by p(AA-co-AM) and p(AA-co-AM)-VEGF showed better integration and wound closure than those treated by suture and Vetbond. On day 10, the skin flaps survived and integrated well with the surrounding tissue without visible pathological inflammation and necrosis. Although the wounds were well closed by suture, the redness and effusion could not be ignored. Moreover, regarding skin color, the skin flap treated with p(AA-co-AM)-VEGF presented a pink appearance, while the distal end of the skin flap treated by suture was cyanotic, indicating tissue ischemia. Hence, p(AA-co-AM)-VEGF had a superior effect on skin flap survival. The Vetbond adhesive group displayed severe red color and scaly lesions on the skin flap from day 3; thus, it was not suitable for the physiological environment of the skin flap.

H&E and Masson's trichrome staining were performed to determine regeneration of the distal part of the skin flap. On postoperative day 5, the suturing and Vetbond adhesive groups showed slight necrosis and poor integration. In contrast, the two film adhesive groups showed no pathological inflammation or scaly lesions on the skin flap. Compared to the other three groups, the side margins of the distal defects were well integrated with the adjacent normal skin tissue in the p(AA-co-AM)-VEGF group (Fig. 6A). After 10 days, hypertrophic epidermis, which is a pathological structure, was observed on one side of the defect in the suturing group. All groups showed good regeneration and integration with dense and thick fiber organization, except for the Vetbond adhesive (Fig. 6B).

Promotion of neovascularization and response to inflammation

Skin flap angiogenesis was examined to determine the neovascularization effect using homogenized tissue enzyme-linked immunosorbent assay (ELISA) test and immunofluorescence staining with CD31 and α–smooth muscle actin (α-SMA). The film of p(AA-co-AM)-VEGF significantly evaluated the content of VEGF in tissue from postoperative day 2 ($P < 0.01$; fig. S7). The vascular maker also verified the neovascularization effect of p(AA-co-AM)-VEGF from the early stage (fig. S8). Ten days after surgery, the density of arterioles in the p(AA-co-AM)-VEGF group was significantly higher than that in the other three groups ($P < 0.05$), and the formation of capillaries was substantially enhanced compared to suturing and Vetbond adhesive (Fig. 7, A and B). Hence, p(AA-co-AM)-VEGF can simultaneously promote wound closure and vascularization.

Polymeric tissue adhesive, as a foreign body, would cause a moderate local inflammatory response in vivo. Mild to moderate inflammatory reactions could give rise to reactive neovascularization, which is beneficial for skin flap survival, but excessive and persistent inflammation inhibits flap recovery (*79*). Macrophages (CD68-positive) and T cells (CD3-positive) play key roles in regulating tissue inflammation and are involved in both acute and chronic inflammation (*76*). Therefore, the percentages of CD68-positive and CD3-positive cells were analyzed. The inflammation level of the p(AA-co-AM) group was enhanced on postoperative day 5, with increased angiogenesis (Fig. 7C). After the film was ejected (day 10), the inflammatory reaction degraded to a normal level (Fig. 7D). In addition, the healing marker fibronectin was almost absent on day 5 in both groups but was elevated on day 10, indicating the regeneration of the skin flap (Fig. 7E). Considering the above factors, the inflammation score was relatively high in the p(AA-co-AM) group on day 5, but the histopathological scores of healing revealed no significant difference between the p(AA-co-AM) and suturing groups across all stages after surgery ($P > 0.05$; Fig. 7F).

In conclusion, we engineered a reversible adhesive to achieve programmable integration and discharge via tunable surface wrinkling patterns. In skin flap transplantation, it successfully substituted for suturing and also served as an effective carrier to precisely deliver the growth factor to the target tissue, thus avoiding systemic side effects and minimizing the required drug dose. The hydrogel film adhesive based on fractal geometry and surface wrinkling patterns sheds light on the biofabrication of tissue adhesives.

MATERIALS AND METHODS

Preparation of dry film adhesive

All the chemicals were acquired from Aladdin and used immediately. To synthesize p(AA-co-AM) copolymer, the different proportion of AA solution (2 mol/liter) and AM solution (2 mol/liter) was mixed. For every per-milliliter mixed solution, 1.9 μl of 3-(trimethoxysilyl)propyl methacrylate (TMSPMA) and 20 μl of V-50 solution (0.1 mol/liter) were added. The solution was then dripped onto an acrylic sheet and spin-coated and subsequently irradiated under ultraviolet light for 15 min. After gelation, it was immersed in HCl solution at pH 3.5 for 5 min, followed by freeze-dried for 5 hours in a vacuum drying oven. The growth factor was loaded onto the surface of dry film adhesive by freeze-drying to fabricate p(AA-co-AM)-VEGF. The final dry film adhesive was sealed in plastic bags with desiccant (silica gel packets) and stored at −20°C before use.

FTIR characterization

An FTIR spectrometer (Thermo Fisher Scientific Nicolet iS5) was used to confirm the chemical composition of the dry film adhesive. FTIR spectra represented the average of 32 scans at a resolution of 4 cm^{-1} between 400 and 4000 cm^{-1}.

Lap shear tests

The fresh porcine skin was chosen as adherend and trimmed into strips with approximately 1.5 cm by 2.5 cm size after rinsed by PBS. Rectangular film adhesives (1 cm by 1 cm) were prepared and placed between two porcine skin tissues. Tests were performed using the universal mechanical testing machine (INSTRON 2710-113) at a constant 20 mm/min speed of extension until the specimens were completely separated. Each tested group contained three samples. Adhesion strength was quantified by dividing the maximum force with the adhesive area.

Measurements of interfacial toughness

The adhesion energy was measured by a 180° peeling test. Two pieces of porcine skin strips (1 cm by 8 cm) were adhered together with the film adhesive. Tests were performed using the universal mechanical testing machine (INSTRON 2710-113) at a constant peeling rate of 20 mm/min. The plateau force is the average force in the plateau region of the force curve, and the interfacial toughness is calculated as 2 × plateau force/width.

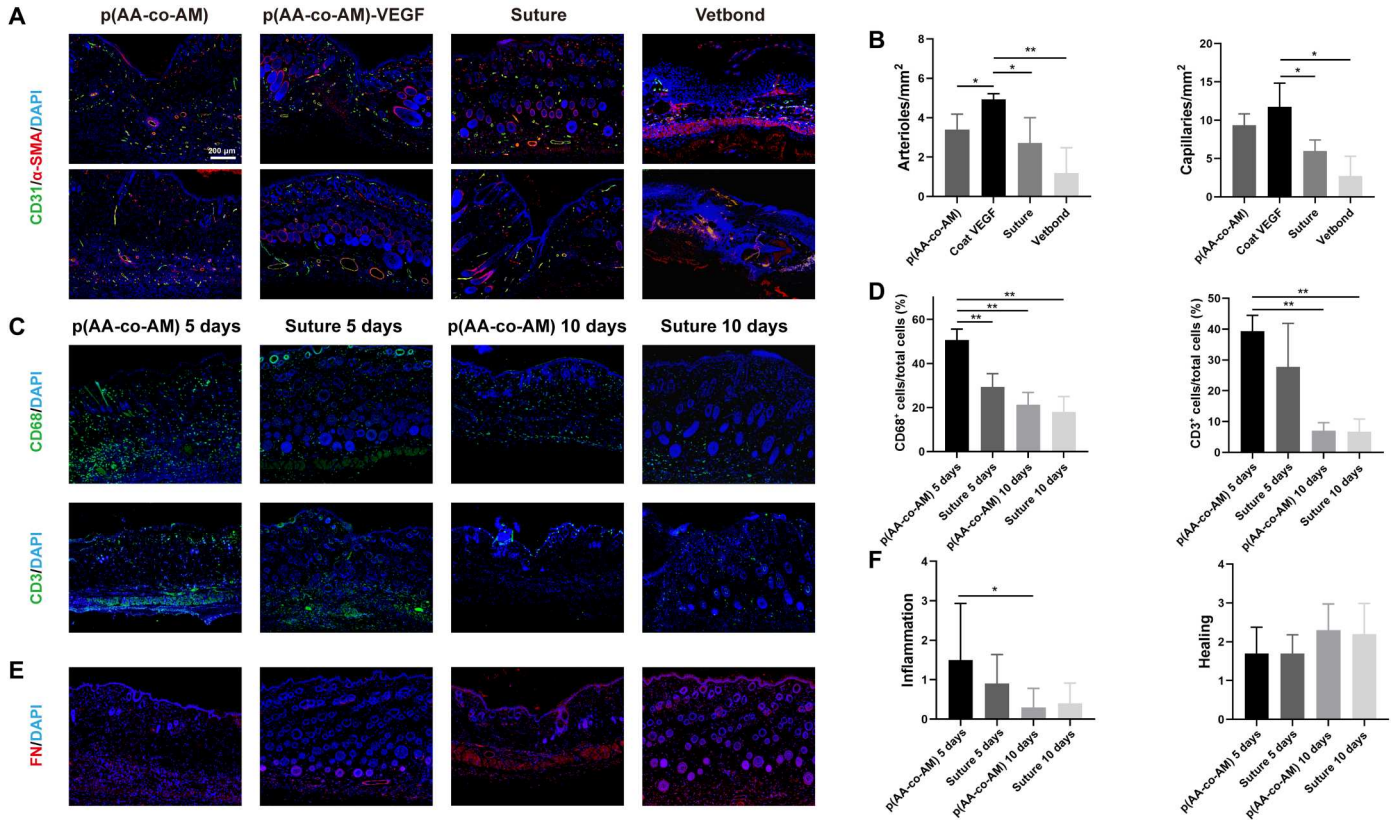

Fig. 7. Healing, vascularization, and inflammation response of skin flap after operation. (**A**) Double immunodetection of CD31-positive (green) and proliferating α-SMA–positive (red) cells in the skin flap. (**B**) Quantification of arterioles and capillaries. (**C**) Immunofluorescence examination of CD68-positive and CD3-positive (inflammatory marker) cells and (**E**) fibronectin (healing marker). (**D**) Quantification of macrophage and T cell percentage. (**F**) Histopathologic scores for healing and inflammation. *$P < 0.05$ and **$P < 0.01$.

Swelling test

The area of prepared dry film adhesives was measured (S_0), and then they were placed in PBS at 37°C. At the predetermined time points, the swollen dry film adhesives were removed from PBS and measured (S_t) after the excess water was wiped off using filter paper. The swelling ratio was determined by the following equation: swelling ratio (%) = $(S_t - S_0)/S_0 \times 100\%$.

SEM characterization

The films were adhered to the skin tissue and then fixed immediately for the observation of the surface morphologies. To mimic tissue fluid exudation in vivo, PBS was added to the gap of the film and tissue and then fixed for the observation of morphology change. For further detecting the interaction between p(AA-co-AM) and attached skin tissue, we performed freeze fracture and SEM examination on the transverse section according to previous reports (*80*). The prepared samples were fixed in 2.5% glutaraldehyde (Solarbio, China) overnight, dehydrated with ethanol, and then critically dried. Next, the samples were fractured manually and coated with gold before SEM detection.

Enzyme-linked immunosorbent assay

For in vitro test, p(AA-co-AM)-VEGF was preserved in PBS at 37°C, while the supernatants were continuously collected at 1 hour, 6 hours, 12 hours, 24 hours, 36 hours, 2 days, 3 days, 4 days, and 5 days. For detecting VEGF release in vivo, the samples of skin flap were collected at 2, 5, 7, and 10 days and mixed with PBS at the ratio of 1:9. The mixture was placed in a tissue homogenizer (Lu kα sample freezing grinder LUKYM-I) to achieve the tissue grinding solution. The supernatant of the tissue grinding solution was collected for detection. These samples were immediately stored at −80°C before detection. An ELISA development kit (Neobioscience) was used to depict the release profile of VEGF according to the instructions.

In vitro cell viability test

CCK-8 assay was conducted to determine the effect of film adhesive extractions on cells. Dermal FBs and HUVECs were previously seeded in 24-well culture plates (5.0×10^3 cells per well), cultured with Dulbecco's modified Eagle's medium overnight, and then treated with p(AA-co-AM) and p(AA-co-AM)-VEGF respectively, which were placed in Transwell chambers. The chambers were removed at the predetermined time points (12, 24, 36, and 48 hours) and added 1 ml of CCK-8. After 1-hour incubation, the absorbance at 450 nm was measured using an ELISA microplate reader (SpectraMax i3x). Besides, a LIVE/DEAD kit (Invitrogen, USA) was used to test cell viability. After 15-min incubation at 37°C, the images were captured by a fluorescence microscope (IX73, Olympus). Cells cultured without the presence of film adhesive were tested as a control.

Bioactivity of released VEGF from adhesive

Tubule formation assay was conducted to analyze the effect of p(AA-co-AM)-VEGF on HUVECs. Briefly, a prechilled 24-well culture plate was previously prepared, and 200 μl of Growth Factor Reduced (GFR) Matrigel (BD Biosciences, USA) was uniformly added to every well, followed by 30-min incubation at 37°C for polymerization. After that, red fluorescent protein —HUVECs were seeded on the GFR-Matrigel (1.0×10^5 cells per well), and p(AA-co-AM) or p(AA-co-AM)-VEGF was placed in a Transwell chamber. The morphology of tube formation was observed with a fluorescence microscope (IX73, Olympus) during 12 hours after incubation.

The same device was applied in scratch assay to determine the effect of p(AA-co-AM)-VEGF on HUVECs′ migration activity. A scarification was made by scratching the cellular monolayer with a 200-μl pipette tip and then rinsed with PBS twice. Then, HUVECs were cultured in a low-serum (2%) medium with p(AA-co-AM)-VEGF in a Transwell chamber. Cells treated with p(AA-co-AM) were cultured as control. After culture for 12 and 24 hours, the morphology was observed under a light microscopy. The migration assay was quantified by the initial scratch area (S_0) and the healing scratch area (S_t) with Image-Pro Plus. The migration percentage was determined by the following equation: migration percentage = $(1 - S_t/S_0) \times 100\%$.

Mouse dorsal skin flap model preparation

The animal study was approved by Nanfang Hospital Animal Ethics Committee Laboratory. Animals in this study were purchased from the Experimental Animal Centre of Southern Medical University (Guangzhou, China). Suturing and commercially available tissue adhesive (3M Vetbond Tissue Adhesive) were used as a control. C57BL6 mice (8 weeks old) were randomly assigned to four groups: p(AA-co-AM) group, p(AA-co-AM)-VEGF group, suture group, and Vetbond adhesive group, respectively. Under sterile conditions, the mice were anesthetized by 1% pentobarbital sodium (50 mg/kg) using intraperitoneal injection. After shaving the hair, the skin flap (2.0 cm × 1.0 cm) was marked on the back. Then, a full-thickness random skin flap was elevated with the pedicle in the tail end, and subsequently, the soft tissue underneath and axial blood vessels connected to the pedicle were completely cut off in the flap. Then, four pieces of dry film adhesive were placed subcutaneously to adhere the flap in situ (Fig. 7A). Mice were euthanized at the predetermined time points, and the skin flaps were collected for further analysis.

In vivo fluorescence imaging

To visualize the in vivo movement of the dry film adhesives, they were labeled with rhodamine B for fluorescence tracing. The photographs were obtained using the In Vivo FX Pro imaging system (Bruker, Madison, WI, USA) at 0, 2, 4, 6 days.

Histological analysis

The extracted skin flap samples were immediately fixed in 4% paraformaldehyde and then transversely cut in the middle. We obtained the distal part of skin flap, as necrosis was easily occurred due to lack of oxygenated blood; thus, it was suitable for analyzing neovascularization. Embedded samples were cut at 5-μm intervals and then stained with H&E and Masson′s trichrome to evaluate flap survival. The morphology of flaps was observed by the optical microscope (BX51, Olympus). Histological assessments were performed by five histopathologists with the blinding method for inflammation (the presence of inflammatory cells and necrosis) and healing (collagen deposition and neovascularization) according to the scoring standard of 0 to 3 (0, none; 1, scant; 2, moderate; and 3, abundant) as previously described.

Immunofluorescence analysis

The samples were prepared as mentioned above. The slides were incubated in the blocking buffer for 1 hour and then stained with the primary mouse-specific antibodies [anti-CD31 (Abcam), 1:100; anti–α-SMA (Abcam), 1:200; anti-fibronectin, 1:100; anti-CD3 (Abcam), 1:100; and anti-CD68 (Abcam), 1:100] at 4°C overnight. Next, the slices were incubated in the secondary antibodies in dark for 1 hour at room temperature and then treated with antifade reagent 4′,6-diamidino-2-phenylindole. Last, the expression of CD31, α-SMA, fibronectin, CD68, and CD3 was evaluated by fluorescence microscopy (BX63, Olympus). The vessels stained with both CD31 and α-SMA were considered as arterioles, while those only positive for CD31 were capillaries.

Statistical analysis

Statistical analysis was conducted with SPSS 26.0 software (SPSS Inc., Chicago, IL, USA). Comparisons between groups were analyzed by the *t* test, as $P < 0.05$ was considered statistically significant ($^*P < 0.05$, $^{**}P < 0.01$, and $^{***}P < 0.001$). Data were presented as means ± SD. All the experiments were performed at least three times.

Supplementary Materials

This PDF file includes:
Supplementary Text
Figs. S1 to S8
Table S1
Legends for movies S1 to S8

Other Supplementary Material for this manuscript includes the following:
Movies S1 to S8

REFERENCES AND NOTES

1. B. Mandelbrot, How long is the coast of britain? Statistical self-similarity and fractional dimension. *Science* **156**, 636–638 (1967).
2. B. Qin, C. Fei, B. Wang, H. A. Stone, N. S. Wingreen, B. L. Bassler, Hierarchical transitions and fractal wrinkling drive bacterial pellicle morphogenesis. *Proc. Natl. Acad. Sci. U.S.A.* **118**, e2023504118 (2021).
3. T. Sun, R. F. Hevner, Growth and folding of the mammalian cerebral cortex: From molecules to malformations. *Nat. Rev. Neurosci.* **15**, 217–232 (2014).
4. G. B. West, J. H. Brown, B. J. Enquist, A general model for the origin of allometric scaling laws in biology. *Science* **276**, 122–126 (1997).
5. C. Li, R. Li, Z. Xu, J. Li, X. Zhang, N. Li, Y. Zhang, Z. Shen, H. Tang, Y. Wang, Packing biomolecules into Sierpiński triangles with global organizational chirality. *J. Am. Chem. Soc.* **143**, 14417–14421 (2021).
6. H. Hou, J. Yin, X. Jiang, Smart patterned surface with dynamic wrinkles. *Acc. Chem. Res.* **52**, 1025–1035 (2019).
7. K. Autumn, Y. A. Liang, S. T. Hsieh, W. Zesch, W. P. Chan, T. W. Kenny, R. Fearing, R. J. Full, Adhesive force of a single gecko foot-hair. *Nature* **405**, 681–685 (2000).
8. K. Autumn, M. Sitti, Y. A. Liang, A. M. Peattie, W. R. Hansen, S. Sponberg, T. W. Kenny, R. Fearing, J. N. Israelachvili, R. J. Full, Evidence for van der Waals adhesion in gecko setae. *Proc. Natl. Acad. Sci. U.S.A.* **99**, 12252–12256 (2002).

9. T. Eisner, D. J. Aneshansley, Defense by foot adhesion in a beetle (*Hemisphaerota cyanea*). *Proc. Natl. Acad. Sci. U.S.A.* **97**, 6568–6573 (2000).
10. J. Huang, M. Juszkiewicz, W. H. de Jeu, E. Cerda, T. Emrick, N. Menon, T. P. Russell, Capillary wrinkling of floating thin polymer films. *Science* **317**, 650–653 (2007).
11. D.-Y. Khang, H. Jiang, Y. Huang, J. A. Rogers, A stretchable form of single-crystal silicon for high-performance electronics on rubber substrates. *Science* **311**, 208–212 (2006).
12. Y. Wang, Z. Shao, W. Zheng, Y. Xie, G. Luo, M. Ding, Q. Liang, A 3D construct of the intestinal canal with wrinkle morphology on a centrifugation configuring microfluidic chip. *Biofabrication* **11**, 045001 (2019).
13. H. Hou, K. Hu, H. Lin, J. Forth, W. Zhang, T. P. Russell, J. Yin, X. Jiang, Reversible surface patterning by dynamic crosslink gradients: Controlling buckling in 2D. *Adv. Mater.* **30**, 1803463 (2018).
14. H. Hou, J. Yin, X. Jiang, Reversible Diels-Alder reaction to control wrinkle patterns: From dynamic chemistry to dynamic patterns. *Adv. Mater.* **28**, 9126–9132 (2016).
15. C. Jiang, L. Zhang, Q. Yang, S. Huang, H. Shi, Q. Long, B. Qian, Z. Liu, Q. Guan, M. Liu, R. Yang, Q. Zhao, Z. You, X. Ye, Self-healing polyurethane-elastomer with mechanical tunability for multiple biomedical applications in vivo. *Nat. Commun.* **12**, 4395 (2021).
16. K. Xu, X. Wu, X. Zhang, M. Xing, Bridging wounds: Tissue adhesives' essential mechanisms, synthesis and characterization, bioinspired adhesives and future perspectives. *Burns. Burns Trauma* **10**, tkac033 (2022).
17. K. Zheng, Q. Gu, D. Zhou, M. Zhou, L. Zhang, Recent progress in surgical adhesives for biomedical applications. *Smart Mater. Med.* **3**, 41–65 (2022).
18. Y. Liu, G. Guan, Y. Li, J. Tan, P. Cheng, M. Yang, B. Li, Q. Wang, W. Zhong, K. Mequanint, C. Zhu, M. Xing, Gelation of highly entangled hydrophobic macromolecular fluid for ultrastrong underwater in situ fast tissue adhesion. *Sci. Adv.* **8**, eabm9744 (2022).
19. Z. Ma, C. Bourquard, Q. Gao, S. Jiang, T. De Iure-Grimmel, R. Huo, X. Li, Z. He, Z. Yang, G. Yang, Y. Wang, E. Lam, Z.-H. Gao, O. Supponen, J. Li, Controlled tough bioadhesion mediated by ultrasound. *Science* **377**, 751–755 (2022).
20. S. Jiang, J. Deng, Y. Jin, B. Qian, W. Lv, Q. Zhou, E. Mei, R. E. Neisiany, Y. Liu, Z. You, J. Pan, Breathable, antifreezing, mechanically skin-like hydrogel textile wound dressings with dual antibacterial mechanisms. *Bioact. Mater.* **21**, 313–323 (2023).
21. H. Yuk, J. Wu, T. L. Sarrafian, X. Mao, C. E. Varela, E. T. Roche, L. G. Griffiths, C. S. Nabzdyk, X. Zhao, Rapid and coagulation-independent haemostatic sealing by a paste inspired by barnacle glue. *Nat. Biomed. Eng.* **5**, 1131–1142 (2021).
22. S. Liu, Z. Luan, T. Wang, K. Xu, Q. Luo, S. Ye, W. Wang, R. Dan, Z. Shu, Y. Huang, K. Mequanint, C. Fan, M. Xing, S. Yang, Endoscopy deliverable and mushroom-cap-inspired hyperboloid-shaped drug-laden bioadhesive hydrogel for stomach perforation repair. *ACS Nano* **17**, 111–126 (2023).
23. Y. Huang, C. Fan, Y. Liu, L. Yang, W. Hu, S. Liu, T. Wang, Z. Shu, B. Li, M. Xing, S. Yang, Nature-derived okra gel as strong hemostatic bioadhesive in human blood, liver, and heart trauma of rabbits and dogs. *Adv. Healthc. Mater.* **11**, e2200939 (2022).
24. Y. Guo, Y. Wang, X. Zhao, X. Li, Q. Wang, W. Zhong, K. Mequanint, R. Zhan, M. Xing, G. Luo, Snake extract-laden hemostatic bioadhesive gel cross-linked by visible light. *Sci. Adv.* **7**, eabf9635 (2021).
25. B. Liu, Y. Wang, Y. Miao, X. Zhang, Z. Fan, G. Singh, X. Zhang, K. Xu, B. Li, Z. Hu, M. Xing, Hydrogen bonds autonomously powered gelatin methacrylate hydrogels with super-elasticity, self-heal and underwater self-adhesion for sutureless skin and stomach surgery and E-skin. *Biomaterials* **171**, 83–96 (2018).
26. P. Wu, D. Chen, H. Yang, C. Lai, C. Xuan, Y. Chen, X. Shi, Antibacterial peptide-modified collagen nanosheet for infected wound repair. *Smart Mater. Med.* **2**, 172–181 (2021).
27. S. Nam, D. Mooney, Polymeric tissue adhesives. *Chem. Rev.* **121**, 11336–11384 (2021).
28. J. M. Korde, B. Kandasubramanian, Biocompatible alkyl cyanoacrylates and their derivatives as bio-adhesives. *Biomater. Sci.* **6**, 1691–1711 (2018).
29. M. Fu, Y. Zhao, Y. Wang, Y. Li, M. Wu, Q. Liu, Z. Hou, Z. Lu, K. Wu, J. Guo, On-demand removable self-healing and pH-responsive europium-releasing adhesive dressing enables inflammatory microenvironment modulation and angiogenesis for diabetic wound healing. *Small* **19**, e2205489 (2023).
30. X. Peng, W. Wang, W. Yang, J. Chen, Q. Peng, T. Wang, D. Yang, J. Wang, H. Zhang, H. Zeng, Stretchable, compressible, and conductive hydrogel for sensitive wearable soft sensors. *J. Colloid Interface Sci.* **618**, 111–120 (2022).
31. D. Sasmal, J. Maity, H. Kolya, T. Tripathy, Selective adsorption of Pb (II) ions by amylopectin-g-*poly* (acrylamide-co-acrylic acid): A bio-degradable graft copolymer. *Int. J. Biol. Macromol.* **97**, 585–597 (2017).
32. D. Das, P. Ghosh, S. Dhara, A. B. Panda, S. Pal, Dextrin and poly(acrylic acid)-based biodegradable, non-cytotoxic, chemically cross-linked hydrogel for sustained release of ornidazole and ciprofloxacin. *ACS Appl. Mater. Interfaces* **7**, 4791–4803 (2015).
33. R. Rizzieri, L. Mahadevan, A. Vaziri, A. Donald, Superficial wrinkles in stretched, drying gelatin films. *Langmuir* **22**, 3622–3626 (2006).
34. E. Sharon, B. Roman, M. Marder, G. S. Shin, H. L. Swinney, Mechanics. Buckling cascades in free sheets. *Nature* **419**, 579 (2002).
35. X. Shi, P. Wu, A smart patch with on-demand detachable adhesion for bioelectronics. *Small* **17**, e2101220 (2021).
36. H. Yuk, C. E. Varela, C. S. Nabzdyk, X. Mao, R. F. Padera, E. T. Roche, X. Zhao, Dry double-sided tape for adhesion of wet tissues and devices. *Nature* **575**, 169–174 (2019).
37. K. Xu, Y. Liu, S. Bu, T. Wu, Q. Chang, G. Singh, X. Cao, C. Deng, B. Li, G. Luo, M. Xing, Egg albumen as a fast and strong medical adhesive glue. *Adv. Healthc. Mater.* **6**, 10.1002/adhm.201700132, (2017).
38. J. Liu, Z. Zheng, J. Luo, P. Wang, G. Lu, J. Pan, Engineered reversible adhesive biofoams for accelerated dermal wound healing: Intriguing multi-covalent phenylboronic acid/cis-diol interaction. *Colloids Surf. B Biointerfaces* **221**, 112987 (2023).
39. M. Chen, Y. Wu, B. Chen, A. M. Tucker, A. Jagota, S. Yang, Fast, strong, and reversible adhesives with dynamic covalent bonds for potential use in wound dressing. *Proc. Natl. Acad. Sci. U.S.A.* **119**, e2203074119 (2022).
40. Y. He, K. Liu, C. Zhang, S. Guo, R. Chang, F. Guan, M. Yao, Facile preparation of PVA hydrogels with adhesive, self-healing, antimicrobial, and on-demand removable capabilities for rapid hemostasis. *Biomater. Sci.* **10**, 5620–5633 (2022).
41. Y.-W. Lee, S. Chun, D. Son, X. Hu, M. Schneider, M. Sitti, A tissue adhesion-controllable and biocompatible small-scale hydrogel adhesive robot. *Adv. Mater.* **34**, e2109325 (2022).
42. X. Fan, Y. Fang, W. Zhou, L. Yan, Y. Xu, H. Zhu, H. Liu, Mussel foot protein inspired tough tissue-selective underwater adhesive hydrogel. *Mater. Horiz.* **8**, 997–1007 (2021).
43. C. Wang, X. Gao, F. Zhang, W. Hu, Z. Gao, Y. Zhang, M. Ding, Q. Liang, Mussel inspired trigger-detachable adhesive hydrogel. *Small* **18**, e2200336 (2022).
44. S. Li, H. Liu, H. Tian, C. Wang, D. Wang, Y. Wu, J. Shao, *Dytiscus lapponicus*-inspired structure with high adhesion in dry and underwater environments. *ACS Appl. Mater. Interfaces* **13**, 42287–42296 (2021).
45. S. Xi, F. Tian, G. Wei, X. He, Y. Shang, Y. Ju, W. Li, Q. Lu, Q. Wang, Reversible dendritic-crystal-reinforced polymer gel for bioinspired adaptable adhesive. *Adv. Mater.* **33**, e2103174 (2021).
46. K. Chen, Q. Lin, L. Wang, Z. Zhuang, Y. Zhang, D. Huang, H. Wang, An all-in-one tannic acid-containing hydrogel adhesive with high toughness, notch insensitivity, self-healability, tailorable topography, and strong, instant, and on-demand underwater adhesion. *ACS Appl. Mater. Interfaces* **13**, 9748–9761 (2021).
47. Y. Chen, Y. Zhang, A. Mensaha, D. Li, Q. Wang, Q. Wei, A plant-inspired long-lasting adhesive bilayer nanocomposite hydrogel based on redox-active Ag/Tannic acid-cellulose nanofibers. *Carbohydr. Polym.* **255**, 117508 (2021).
48. X. Chen, H. Yuk, J. Wu, C. S. Nabzdyk, X. Zhao, Instant tough bioadhesive with triggerable benign detachment. *Proc. Natl. Acad. Sci. U.S.A.* **117**, 15497–15503 (2020).
49. Y. Gao, K. Wu, Z. Suo, Photodetachable adhesion. *Adv. Mater.* **31**, e1806948 (2019).
50. R. Xu, S. Ma, Y. Wu, H. Lee, F. Zhou, W. Liu, Adaptive control in lubrication, adhesion, and hemostasis by Chitosan-Catechol-pNIPAM. *Biomater. Sci.* **7**, 3599–3608 (2019).
51. J. Xu, G. Wang, Y. Wu, X. Ren, G. Gao, Ultrastretchable wearable strain and pressure sensors based on adhesive, tough, and self-healing hydrogels for human motion monitoring. *ACS Appl. Mater. Interfaces* **11**, 25613–25623 (2019).
52. X. Di, Y. Kang, F. Li, R. Yao, Q. Chen, C. Hang, Y. Xu, Y. Wang, P. Sun, G. Wu, Poly(*N*-isopropylacrylamide)/polydopamine/clay nanocomposite hydrogels with stretchability, conductivity, and dual light- and thermo- responsive bending and adhesive properties. *Colloids Surf. B Biointerfaces* **177**, 149–159 (2019).
53. L. Guan, S. Yan, X. Liu, X. Li, G. Gao, Wearable strain sensors based on casein-driven tough, adhesive and anti-freezing hydrogels for monitoring human-motion. *J. Mater. Chem. B* **7**, 5230–5236 (2019).
54. S. Baik, D. W. Kim, Y. Park, T. J. Lee, S. Ho Bhang, C. Pang, A wet-tolerant adhesive patch inspired by protuberances in suction cups of octopi. *Nature* **546**, 396–400 (2017).
55. S. Baik, H. J. Lee, D. W. Kim, H. Min, C. Pang, Capillarity-enhanced organ-attachable adhesive with highly drainable wrinkled octopus-inspired architectures. *ACS Appl. Mater. Interfaces* **11**, 25674–25681 (2019).
56. Y. Ma, S. Ma, Y. Wu, X. Pei, S. N. Gorb, Z. Wang, W. Liu, F. Zhou, Remote control over underwater dynamic attachment/detachment and locomotion. *Adv. Mater.* **30**, e1801595 (2018).
57. Y. Yan, J. Huang, X. Qiu, X. Cui, S. Xu, X. Wu, P. Yao, C. Huang, An ultra-stretchable glycerol-ionic hybrid hydrogel with reversible gelid adhesion. *J. Colloid Interface Sci.* **582**, 187–200 (2021).
58. J. Mu, C. Hou, G. Wang, X. Wang, Q. Zhang, Y. Li, H. Wang, M. Zhu, An elastic transparent conductor based on hierarchically wrinkled reduced graphene oxide for artificial muscles and sensors. *Adv. Mater.* **28**, 9491–9497 (2016).
59. J. Y. Chung, A. J. Nolte, C. M. Stafford, Surface wrinkling: A versatile platform for measuring thin-film properties. *Adv. Mater.* **23**, 349–368 (2011).

60. I. Ozyazgan, N. Liman, N. Dursun, I. Gunes, The effects of ovariectomy on the mechanical properties of skin in rats. *Maturitas* **43**, 65–74 (2002).
61. E. Cerda, L. Mahadevan, Geometry and physics of wrinkling. *Phys. Rev. Lett.* **90**, 074302 (2003).
62. J. Yin, Z. Cao, C. Li, I. Sheinman, X. Chen, Stress-driven buckling patterns in spheroidal core/shell structures. *Proc. Natl. Acad. Sci. U.S.A.* **105**, 19132–19135 (2008).
63. S. Chung, R. Sudo, I. K. Zervantonakis, T. Rimchala, R. D. Kamm, Surface-treatment-induced three-dimensional capillary morphogenesis in a microfluidic platform. *Adv. Mater.* **21**, 4863–4867 (2009).
64. Y. Tan, B. Hu, J. Song, Z. Chu, W. Wu, Bioinspired multiscale wrinkling patterns on curved substrates: An overview. *Nanomicro. Lett.* **12**, 101 (2020).
65. H. Nishimori, N. Ouchi, Formation of ripple patterns and dunes by wind-blown sand. *Phys. Rev. Lett.* **71**, 197–200 (1993).
66. P. J. Yoo, K. Y. Suh, H. Kang, H. H. Lee, Polymer elasticity-driven wrinkling and coarsening in high temperature buckling of metal-capped polymer thin films. *Phys. Rev. Lett.* **93**, 034301 (2004).
67. M. Guvendiren, J. A. Burdick, The control of stem cell morphology and differentiation by hydrogel surface wrinkles. *Biomaterials* **31**, 6511–6518 (2010).
68. L. Pocivavsek, R. Dellsy, A. Kern, S. Johnson, B. Lin, K. Y. Lee, E. Cerda, Stress and fold localization in thin elastic membranes. *Science* **320**, 912–916 (2008).
69. K. Efimenko, M. Rackaitis, E. Manias, A. Vaziri, L. Mahadevan, J. Genzer, Nested self-similar wrinkling patterns in skins. *Nat. Mater.* **4**, 293–297 (2005).
70. M. Tapia-Albarran, L. Villafuerte-Robles, Effect of formulation and process variables on the release behavior of amoxicillin matrix tablets. *Drug Dev. Ind. Pharm.* **30**, 901–908 (2004).
71. X. Mao, L. Liu, L. Cheng, R. Cheng, L. Zhang, L. Deng, X. Sun, Y. Zhang, B. Sarmento, W. Cui, Adhesive nanoparticles with inflammation regulation for promoting skin flap regeneration. *J. Control Release* **297**, 91–101 (2019).
72. Y. Jiang, X. Zhang, W. Zhang, M. Wang, L. Yan, K. Wang, L. Han, X. Lu, Infant skin friendly adhesive hydrogel patch activated at body temperature for bioelectronics securing and diabetic wound healing. *ACS Nano* **16**, 8662–8676 (2022).
73. Y. Liang, Z. Li, Y. Huang, R. Yu, B. Guo, Dual-dynamic-bond cross-linked antibacterial adhesive hydrogel sealants with on-demand removability for post-wound-closure and infected wound healing. *ACS Nano* **15**, 7078–7093 (2021).
74. Y. Liang, H. Xu, Z. Li, A. Zhangji, B. Guo, Bioinspired injectable self-healing hydrogel sealant with fault-tolerant and repeated thermo-responsive adhesion for sutureless post-wound-closure and wound healing. *Nanomicro. Lett.* **14**, 185 (2022).
75. L. K. Borden, A. Gargava, S. R. Raghavan, Reversible electroadhesion of hydrogels to animal tissues for suture-less repair of cuts or tears. *Nat. Commun.* **12**, 4419 (2021).
76. X. Mao, R. Cheng, H. Zhang, J. Bae, L. Cheng, L. Zhang, L. Deng, W. Cui, Y. Zhang, H. A. Santos, X. Sun, Self-healing and injectable hydrogel for matching skin flap regeneration. *Adv. Sci. (Weinh)* **6**, 1801555 (2019).
77. M. S. Lee, T. Ahmad, J. Lee, H. K. Awada, Y. Wang, K. Kim, H. Shin, H. S. Yang, Dual delivery of growth factors with coacervate-coated poly(lactic-co-glycolic acid) nanofiber improves neovascularization in a mouse skin flap model. *Biomaterials* **124**, 65–77 (2017).
78. S. M. Seyed Jafari, M. Shafighi, H. Beltraminelli, T. Geiser, R. E. Hunger, A. Gazdhar, Improvement of flap necrosis in a rat random skin flap model by in vivo electroporation-mediated hgf gene transfer. *Plast. Reconstr. Surg.* **139**, 1116e–1127e (2017).
79. K. Zheng, W. Niu, B. Lei, A. R. Boccaccini, Immunomodulatory bioactive glasses for tissue regeneration. *Acta Biomater.* **133**, 168–186 (2021).
80. N. Lang, M. J. Pereira, Y. Lee, I. Friehs, N. V. Vasilyev, E. N. Feins, K. Ablasser, E. D. O'Cearbhaill, C. Xu, A. Fabozzo, R. Padera, S. Wasserman, F. Freudenthal, L. S. Ferreira, R. Langer, J. M. Karp, P. J. del Nido, A blood-resistant surgical glue for minimally invasive repair of vessels and heart defects. *Sci. Transl. Med.* **6**, 218ra6 (2014).

Acknowledgments

Funding: This study was supported by the National Natural Science Foundation of China (grant nos. 81701929, 82172235 and 81971889) and by the Natural Science Foundation of Guangdong Province (grant nos. 2019A1515012170 and 2020A1515010565). M.X. thanks the support from the Discovery grant of Natural Sciences and Engineering Research Council of Canada. **Author contributions:** M.X., Y.M., L.W., and Z.H. conceived and designed the research. M.X. generated the idea. Y.Z., L.Y., Q.W., and Y.S. performed the manufacturing, mechanical characterization, and in vitro testing of the adhesive. Y.Z., Z.L., J.H., and B.L. performed the in vivo experiments. Y.Z., M.X., Y.M., and Z.H. analyzed the results and wrote the manuscript. All authors discussed the results and approved the manuscript. **Competing interests:** The authors declare that they have no competing interests. **Data and materials availability:** All data needed to evaluate the conclusions in the paper are present in the paper and/or the Supplementary Materials.

Submitted 29 September 2022
Accepted 10 March 2023
Published 12 April 2023
10.1126/sciadv.adf1043